Chinese Physics B

RAPID COMMUNICATION

Observation of parabolic electron bands on superconductor $LaRu_2As_2$

To cite this article: Xingtai Zhou *et al* 2024 *Chinese Phys. B* **33** 077401

RAPID COMMUNICATION

Observation of parabolic electron bands on superconductor $LaRu_2As_2$

Xingtai Zhou(周兴泰)[1,2], Geng Li(李更)[1,2,3,†], Lulu Pan(潘禄禄)[1,2], Zichao Chen(陈子超)[1,2], Meng Li(李萌)[1,2], Yanhao Shi(时延昊)[1,2], Haitao Yang(杨海涛)[1,2], and Hong-Jun Gao(高鸿钧)[1,2,3]

[1] *Beijing National Center for Condensed Matter Physics and Institute of Physics, Chinese Academy of Sciences, Beijing* 100190, *China*
[2] *School of Physical Sciences, University of Chinese Academy of Sciences, Beijing* 100190, *China*
[3] *Hefei National Laboratory, Hefei* 230088, *China*

(Received 7 April 2024; revised manuscript received 10 May 2024; accepted manuscript online 20 May 2024)

Ru-based superconductor $LaRu_2As_2$ has been discovered exhibiting the highest critical temperature of ~ 7.8 K among iron-free transition metal pnictides with the $ThCr_2Si_2$-type crystal structure. However, microscopic research on this novel superconducting material is still lacking. Here, we utilize scanning tunneling microscopy/spectroscopy to uncover the superconductivity and surface structure of $LaRu_2As_2$. Two distinct terminating surfaces are identified on the cleaved crystals, namely, the As surface and the La surface. Atomic missing line defects are observed on the La surface. Both surfaces exhibit a superconducting gap of ~ 1.0 meV. By employing quasiparticle interference techniques, we observe standing wave patterns near the line defects on the La atomic plane. These patterns are attributed to quasiparticle scattering from two electron type parabolic bands.

Keywords: superconductivity, line defect, quasi-particle scattering, electron band

PACS: 74.70.–b, 03.75.Lm, 68.37.–d, 68.35.Dv **DOI:** 10.1088/1674-1056/ad4d63

1. Introduction

Recently, the ternary $ThCr_2Si_2$-type compound $LaRu_2As_2$ has been discovered to exhibit superconductivity with a critical temperature (T_c) of ~ 7.8 K.[1] Given its structural similarity to AFe_2As_2 (A = K, Na, Ba, ...), it was expected that Ru-based superconductors would exhibit properties comparable to iron-based superconductors.[2–14] In certain complex AFe_2As_2 systems, such as K-doped $BaFe_2As_2$, researchers have utilized muon spin rotation (μSR) techniques to confirm the presence of a time-reversal symmetry breaking superconducting state.[15–18] These findings suggest the potential existence of novel superconducting properties within materials sharing the AFe_2As_2-like structure. According to ^{75}As-nuclear magnetic resonance (NMR) and nuclear quadrupole resonance (NQR) experiments, $LaRu_2As_2$ was indicated to be a fully gaped type-II superconductor.[19–21]

Although there have been investigations about the bulk properties of $LaRu_2As_2$, utilizing techniques such as transport measurements and the first principles calculation,[1,22,23] the microscopic properties of $LaRu_2As_2$ remain unexplored. To gain deeper insights into the spectroscopic characteristics of this novel Ru-based superconductor, we utilize scanning tunneling microscopy/spectroscopy (STM/S) to examine the cleaved $LaRu_2As_2$ surface. Our results demonstrate unconventional superconducting behavior of the crystal. Furthermore, we observe atomic missing line defects on the La surfaces which lead to distinct standing wave patterns. The quasiparticle interference (QPI) analysis demonstrates the existence of free-electron like parabolic bands. Our findings add new insight into understanding the inherent physical properties of $LaRu_2As_2$.

2. Experimental details

2.1. Single-crystal growth

High-quality $LaRu_2As_2$ single crystals were synthesized by using the Bi-flux method. A $LaRu_2As_2$ crystal was mounted on an STM sample holder in a glove box and transferred to an ultra-high vacuum chamber. The crystal was cleaved *in-situ* at room temperature, and then immediately transferred to an STM scanner.

2.2. STM/S experiments

The STM/S measurements were conducted in an ultra-low temperature STM system equipped with 9-2-2 T vectorial magnets. Tungsten tips were etched chemically and calibrated on Au(111) surfaces before use. The $\mathrm{d}I/\mathrm{d}V$ spectra and maps were obtained by a standard lock-in technique with modulation voltage of 0.1 mV in Fig. 2 and 10 mV in Figs. 3 and 4 at 973.1 Hz. All the images and $\mathrm{d}I/\mathrm{d}V$ maps were taken at 400 mK.

†Corresponding author. E-mail: gengli.iop@iphy.ac.cn

3. Results and discussion

The ternary compound $LaRu_2As_2$ belongs to the $I4/mmm$ (No. 139) space group, with lattice constants of $a = 4.18$ Å and $c = 10.59$ Å.[1] Similar to the crystal structure of other 122 family materials, the La atoms and Ru–As layers arrange alternately (Fig. 1(a)). In order to verify the chemical composition of the sample, we conducted energy dispersive x-ray (EDX) spectroscopy on the as-grown single crystal (Fig. 1(b)). The proportions of La, Ru, and As elements are determined to be ∼ 1:2.12:2.12, consistent with the chemical formula of the single crystal but with a relative lack of La. X-ray diffraction (XRD) analysis confirms the single crystal nature of the sample (Fig. 1(c)). Additionally, the small full width at half maximum (FWHM) of the rocking curve, illustrated in Fig. 1(d), serves as further evidence of the high quality of the sample. High-angle annular dark-field (HAADF) image measured with the electron beam along [100] axis (Fig. 1(e)) and the corresponding selected area electron diffraction (SAED) image (Fig. 1(f)) show direct evidence of a perfect match between the as-grown sample and the crystal model in Fig. 1(a). To uncover the superconducting behavior of the sample, we performed transport measurement, which suggests a superconducting transition temperature $T_c \sim 2.6$ K (Fig. 1(g)). The difference of T_c between our sample and those in previous reports is attributed to possible defect during growth,[1,19] as our EDX spectroscopy indicates relative lack of La in the compound (Fig. 1(b)).

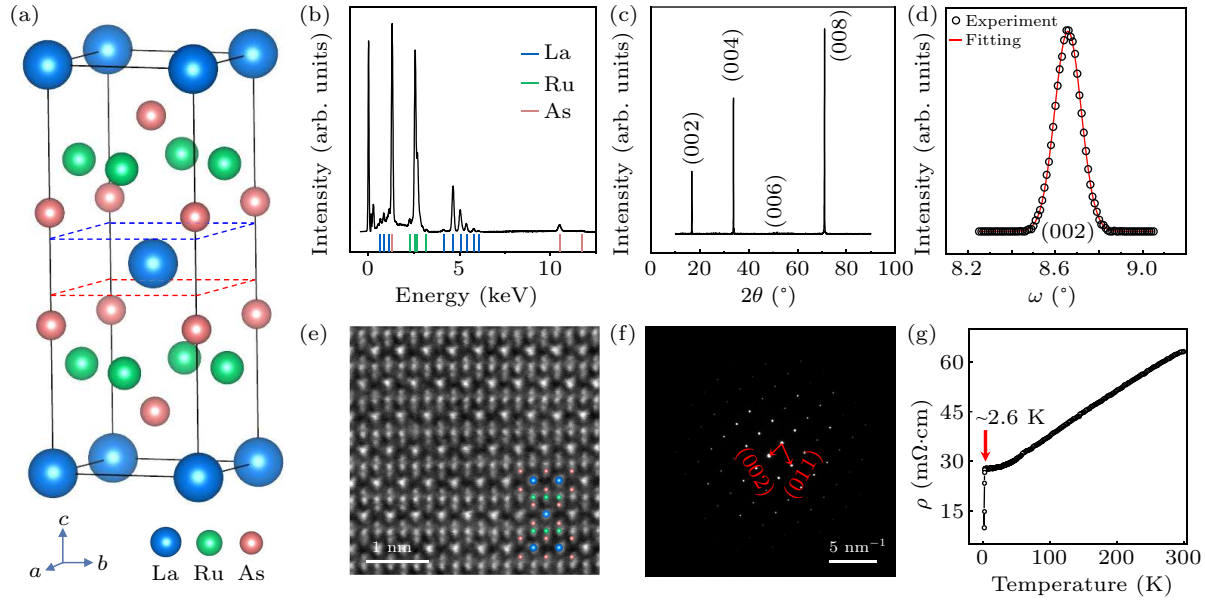

Fig. 1. Crystal structure and transport measurement of $LaRu_2As_2$. (a) Schematic of crystal structure of $LaRu_2As_2$. (b) EDX spectroscopy of the as-grown single crystal. The chemical composition of La:Ru:As is determined to be 1:2.12:2.12. (c) XRD pattern (θ–2θ scan) of the $LaRu_2As_2$ single crystal, showing the peaks of the {001} crystal planes family. The lattice constant is determined to be $c = 10.055$ Å. (d) Rocking curve measured on the (002) peak showing a FWHM ∼ 0.142°, which indicates the high quality of the single crystal. (e) HAADF image measured with the electron beam along [100] axis. The La, Ru and As atoms are overlaid to guide the eye. (f) The corresponding SAED image, showing sharp diffraction spots of the crystal. (g) Temperature-dependent longitudinal resistivity (ρ–T) curve of the $LaRu_2As_2$ single crystal from 300 K to 2 K under zero external magnetic field. The dramatic drop of the resistivity at low temperature indicates that the onset critical temperature of superconductivity is ∼ 2.6 K.

A single crystal of $LaRu_2As_2$ was cleaved in an ultra-high vacuum at room temperature and promptly transferred to the scanner for low-temperature measurements. Figure 2(a) shows a representative large-scale STM topography of $LaRu_2As_2$. Two distinct types of terminating surfaces, the La surface and the As surface, are observed due to different cleaving planes (dashed lines in Fig. 1(a)), a phenomenon commonly seen in the 122 family.[24–27] The two surfaces differ significantly in topography. On the La surface, atomic missing line defects are frequently observed (left part in Fig. 2(a)). Residual La clusters, appearing as bright dots, are visible on the As surface (middle part in Fig. 2(a)). The height profile (Fig. 2(b)) along the black dashed line in Fig. 2(a) reveals that the height difference between the lower and higher La surfaces matches the value of half a unit cell along c axis. The atomically resolved image of the As surface (Fig. 2(c)) reveals perfect square lattice despite the presence of atomic defects. The lattice constant measured on the As surface is ∼ 0.42 nm, consistent with previous reports[1] and our HAADF measurement results. On the La surface, however, the individual atoms are difficult to resolve (Fig. 2(d)), likely due to the extended wavefunctions of the metallic surface.[28]

To study the superconducting properties of the two terminating surfaces, we performed scanning tunneling spectra on the surfaces at 0.4 K (Fig. 2(e)). While both surfaces give V-

shaped feature with superconducting gap of ~ 0.96 meV on the As surface and ~ 0.98 meV on the La surface, less contribution from the in-gap states is identified on the As surface, which may be due to different doping levels on the two surfaces. Such a small gap is consistent with a reduced superconducting transition temperature of 2.6 K. The dramatically reduced T_c is also responsible for the V-shape of the superconducting spectra, given that the effective temperature of our equipment is ~ 0.8 K.[9,12] Despite these unexpected results, the superconductivity seems to be homogeneous on the two surfaces (Figs. 2(g) and 2(h)).

The defect also affects the critical field of $LaRu_2As_2$. We applied a magnetic field perpendicular to the sample surface and monitored the changes in the superconducting spectrum. As the magnetic field increases, the magnitude of the superconducting energy gap as well as the intensity of the superconducting coherence peaks gradually decreases (Fig. 2(f)). Ultimately, at around 4 T, the superconducting energy gap completely vanishes, suggesting a superconducting critical field of ~ 4 T. This result significantly differs from the previously reported critical field of about 1.6 T in transport measurements, further confirming the influence of the defects which pin the magnetic fields.

Remarkably, atomic missing line defects along high symmetry direction are commonly seen on the La surface (Fig. 3(a)).[29] We performed a $\mathrm{d}I/\mathrm{d}V$ linecut across a surface line defect, indicated by the dashed arrow in Fig. 3(a). The corresponding intensity plot and the waterfall-like plot of the $\mathrm{d}I/\mathrm{d}V$ linecut are shown in Figs. 3(b) and 3(c), respectively. The $\mathrm{d}I/\mathrm{d}V$ spectra taken far from any surface defects exhibit several prominent peaks at the positive bias side. As we approach the line defects from distant positions, these peaks gradually shift away from the Fermi energy, eventually forming a ripple-like pattern on both sides of the line defects, as shown in Fig. 3(b). To highlight the distinctions among the $\mathrm{d}I/\mathrm{d}V$ spectra at various positions on the La surface, we compare typical spectra at the line defect position (green) and another at a location far from the line defect (red), as depicted in Fig. 3(d). At the distant position from the defect, we observed several notable peaks on the positive bias side, located near 100 meV, 540 meV, and 800 meV, respectively. However, at the line defect position, these peaks shift away from the Fermi surface and form a ripple-like pattern in the intensity plot.

Quasiparticle interference (QPI) is a useful technique in scanning tunneling microscopy that allows for the indirect acquisition of momentum information by performing a Fourier transform (FT) on real-space patterns.[30–34] We therefore perform a Fourier transform on the linecut in Fig. 3(b), and obtain the relationship between the momentum k of the quasiparticles near the line defect and the energy, as shown in Fig. 3(e). A notable feature of the QPI pattern is the clear observation of two parabolic electron-type energy bands on the unoccupied state, with the bottoms situating at approximately 50 meV and 600 meV, respectively. This straightforward method enables us to obtain the surface band structure of the sample. It is worth mentioning that similar scattering phenomena are not limited to the vicinity of the line defect on the La surface. We also observed similar ripple-like scattering patterns near two adjacent La surface terraces where the steps act as scattering centers.

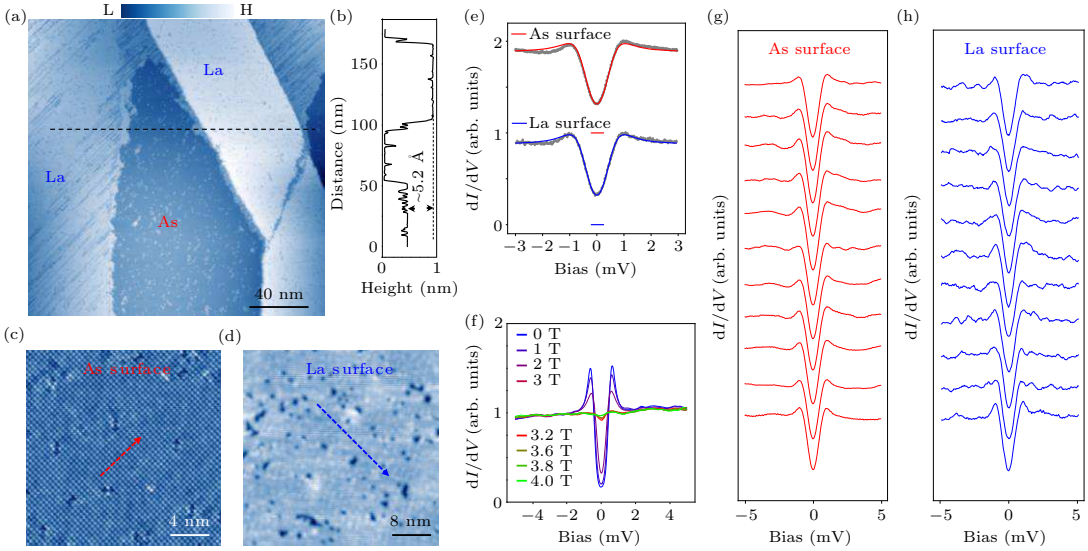

Fig. 2. STM topography and scanning tunneling spectra of $LaRu_2As_2$. (a) Large scale STM image of $LaRu_2As_2$, showing surfaces terminating at the La and As atomic planes. (b) Height profile along the black dashed line in panel (a). (c) Atomically resolved STM image of the As surface. (d) Typical STM topography of the La surface. (e) Averaged $\mathrm{d}I/\mathrm{d}V$ spectra and fitting results on the As surface (red) and the La surface (blue), showing a superconducting gap of ~ 0.96 meV on the As surface and ~ 0.98 meV on the La surface. (f) Averaged $\mathrm{d}I/\mathrm{d}V$ spectra of the As surface under different magnetic fields. (g) and (h) Waterfall-like $\mathrm{d}I/\mathrm{d}V$ spectra linecut along the dashed arrows in panels (c) and (d), respectively, showing homogeneous superconductivity on the surfaces.

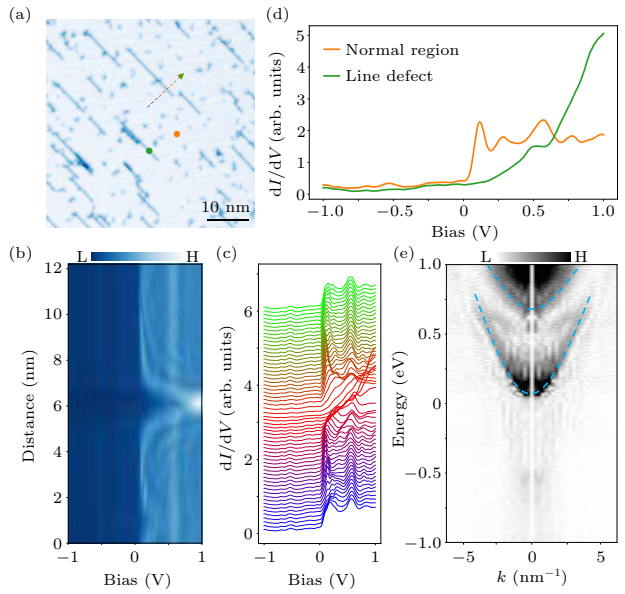

Fig. 3. Scanning tunneling spectra across an atomic missing line defect. (a) STM topography of the La surface with atomic missing line defects. (b) $\mathrm{d}I/\mathrm{d}V$ line-cut intensity plot along the dashed arrow in panel (a). (c) Waterfall-like plot of panel (b). (d) $\mathrm{d}I/\mathrm{d}V$ spectra on the surface line defect (green) and away from defects (orange), as marked in panel (a). (e) The band structure obtained by the Fourier transform of panel (b). The two dashed lines outline the electron bands.

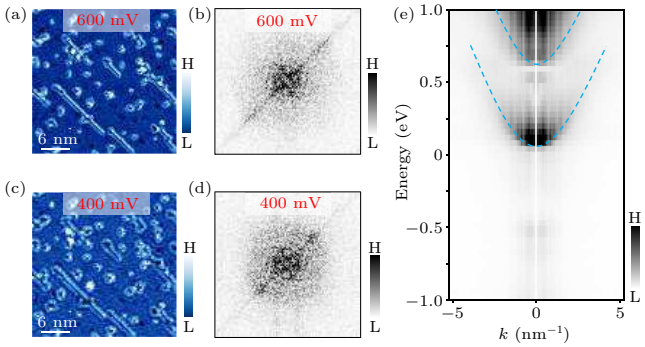

Fig. 4. QPI analysis on the La surface. (a) and (b) $\mathrm{d}I/\mathrm{d}V$ map of a typical region on the La surface at 600 mV (a) and its corresponding FT image (b), showing scattering patterns around the defects. (c) and (d) $\mathrm{d}I/\mathrm{d}V$ map of the same region in (a) but at 400 mV (c) and its corresponding FT image (d). (e) The band structure reconstructed from the QPI. The two dashed lines outline the electron bands.

To further validate the obtained band structure from scattering at the line defect, we performed traditional two-dimensional QPI experiments on the La surface that contains abundant line defects. Figures 4(a) and 4(c) display the maps of differential conductance at different energies, along with their corresponding FT images (Figs. 4(b) and 4(d)). In the differential conductance maps, the characteristic ripple-like scattering patterns around the line defects are clearly visible. These ripples exhibit varying periods at different energies, and the magnitude of the wave vector in the corresponding FT images gradually changes. At 400 meV, the scattering period in the differential conductance map is larger, indicating a smaller wave vector in reciprocal space. However, at 600 meV, the shorter scattering period corresponds to a larger wave vector. This change is consistent with the electron-type band at the position with a band bottom of 50 meV. Above 600 meV, the scattering wave vector again reaches a minimum, corresponding to the electron-type energy band with a band bottom at 600 meV. By combining the scattering wave vectors obtained at different energies, we are able to construct the energy band structure, as depicted in Fig. 4(e). Again, we clearly observe two parabolic electron-type energy bands, consistent with the results obtained from the line defects and terrace edges on the La surface. These findings further strengthen the consistency between the band structures obtained from different techniques and locations on the La surface.

4. Conclusion

We observed two distinct terminating surfaces: the As surface with atomic resolution and the La surface with atomic missing line defects. Both surfaces exhibit a uniform superconducting gap at low temperatures, with a gap size of ~ 1.0 meV. The superconducting gap decreases gradually with increasing magnetic fields, and completely vanishes at around 4 T. The lower transition temperature and higher critical magnetic field can be attributed to impurities present during the sample growth process and/or the imperfect crystallinity of the material. Additionally, we observed a ripple-like modulation of the electronic density of state on the line defects of the La surface. Using QPI technology, we analyzed the scattering near the defects and attributed it to the presence of two parabolic electron-type energy bands in the unoccupied state. Overall, these findings provide valuable insights into the surface properties and superconducting behavior of the $LaRu_2As_2$ sample, advancing our understanding of its electronic structure and potential applications in the future.

Acknowledgments

Project supported by the National Natural Science Foundation of China (Grant Nos. 62488201 and 52072401), the National Key R&D Program of China (Grant No. 2019YFA0308500), the Chinese Academy of Sciences (Grant No. YSBR-003), and the Innovation Program of Quantum Science and Technology (Grant No. 2021ZD0302700).

References

[1] Guo Q, Pan B J, Yu J, Ruan B B, Chen D Y, Wang X C, Mu Q G, Chen G F and Ren Z A 2016 *Sci. Bull.* **61** 921
[2] Fernandes R M, Coldea A I, Ding H, Fisher I R, Hirschfeld P J and Kotliar G 2022 *Nature* **601** 35
[3] Li G, Li M, Zhou X and Gao H J 2024 *Rep. Prog. Phys.* **87** 016501
[4] Li G, Zhu S, Wang D, Wang Y and Gao H J 2021 *Supercond. Sci. Technol.* **34** 073001
[5] Li G, Zhu S, Fan P, Cao L and Gao H J 2022 *Chin. Phys. B* **31** 080301
[6] Rotter M, Tegel M and Johrendt D 2008 *Phys. Rev. Lett.* **101** 107006

[7] Sasmal K, Lv B, Lorenz B, Guloy A M, Chen F, Xue Y Y and Chu C W 2008 *Phys. Rev. Lett.* **101** 107007

[8] Torikachvili M S, Bud'ko S L, Ni N and Canfield P C 2008 *Phys. Rev. Lett.* **101** 057006

[9] Li M, Li G, Cao L, Zhou X, Wang X, Jin C, Chiu C K, Pennycook S J, Wang Z and Gao H J 2022 *Nature* **606** 890

[10] Liu W, Cao L, Zhu S, Kong L, Wang G, Papaj M, Zhang P, Liu Y B, Chen H, Li G, Yang F, Kondo T, Du S, Cao G H, Shin S, Fu L, Yin Z, Gao H J and Ding H 2020 *Nat. Commun.* **11** 5688

[11] Kong L, Cao L, Zhu S, Papaj M, Dai G, Li G, Fan P, Liu W, Yang F, Wang X, Du S, Jin C, Fu L, Gao H J and Ding H 2021 *Nat. Commun.* **12** 4146

[12] Fan P, Chen H, Zhou X, Cao L, Li G, Li M, Qian G, Xing Y, Shen C, Wang X, Jin C, Gu G, Ding H and Gao H J 2023 *Nano Lett.* **23** 4541

[13] Wang X, Gong D, Liu B, Ma X, Zhao J, Wang P, Sheng Y, Guo J, Sun L, Zhang W, Lai X, Tan S, Yang Y and Li S 2022 *Chin. Phys. Lett.* **39** 107101

[14] Li J, Phan G N, Wang X, Yang F, Hu Q, Jia K, Zhao J, Liu W, Zhang R, Shi Y, Li S, Qian T and Ding H 2023 *Chin. Phys. B* **33** 017401

[15] Grinenko V, Materne P, Sarkar R, Luetkens H, Kihou K, Lee C H, Akhmadaliev S, Efremov D V, Drechsler S L and Klauss H H 2017 *Phys. Rev. B* **95** 214511

[16] Grinenko V, Sarkar R, Kihou K, Lee C H, Morozov I, Aswartham S, Büchner B, Chekhonin P, Skrotzki W, Nenkov K, Hühne R, Nielsch K, Drechsler S L, Vadimov V L, Silaev M A, Volkov P A, Eremin I, Luetkens H and Klauss H H 2020 *Nat. Phys.* **16** 789

[17] Iguchi Y, Shi R A, Kihou K, Lee C H, Barkman M, Benfenati A L, Grinenko V, Babaev E and Moler K A 2023 *Science* **380** 1244

[18] Zhao S Z, Song H Y, Hu L L, Xie T, Liu C, Luo H Q, Jiang C Y, Zhang X, Nie X C, Meng J Q, Duan Y X, Liu S B, Xie H Y and Liu H Y 2020 *Phys. Rev. B* **102** 144519

[19] Luo J, Wang C, Wang Z, Guo Q, Yang J, Zhou R, Matano K, Oguchi T, Ren Z, Cao G and Zheng G Q 2020 *Chin. Phys. B* **29** 067402

[20] Goodman B B 1966 *Rep. Prog. Phys.* **29** 445

[21] Rosenstein B and Li D 2010 *Rev. Mod. Phys.* **82** 109

[22] Hadi M A, Ali M S, Naqib S H and Islam A K M A 2017 *Chin. Phys. B* **26** 037103

[23] Rahaman Md Z and Rahman Md A 2017 *J. Alloys Compd.* **695** 2827

[24] Cao L, Song Y, Liu Y B, Zheng Q, Han G, Liu W, Li M, Chen H, Xing Y, Cao G H, Ding H, Lin X, Du S, Zhang Y Y, Li G, Wang Z and Gao H J 2021 *Nano Res.* **14** 3921

[25] Li A, Yin J X, Wang J, Wu Z, Ma J, Sefat A S, Sales B C, Mandrus D G, McGuire M A, Jin R, Zhang C, Dai P, Lv B, Chu C W, Liang X, Hor P H, Ting C S and Pan S H 2019 *Phys. Rev. B* **99** 134520

[26] Nascimento V B, Li A, Jayasundara D R, Xuan Y, O'Neal J, Pan S, Chien T Y, Hu B, He X B, Li G, Sefat A S, McGuire M A, Sales B C, Mandrus D, Pan M H, Zhang J, Jin R and Plummer E W 2009 *Phys. Rev. Lett.* **103** 076104

[27] Liu X, Tao R, Ren M, Chen W, Yao Q, Wolf T, Yan Y, Zhang T and Feng D 2019 *Nat. Commun.* **10** 1039

[28] Marshall M S J, Newell D T, Payne D J, Egdell R G and Castell M R 2011 *Phys. Rev. B* **83** 035410

[29] Liu Y, Wei T, He G, Zhang Y, Wang Z and Wang J 2023 *Nature* **618** 934

[30] Lee W C, Wu C, Arovas D P and Zhang S C 2009 *Phys. Rev. B* **80** 245439

[31] Crommie M F, Lutz C P and Eigler D M 1993 *Nature* **363** 524

[32] Hoffman J E, McElroy K, Lee D H, Lang K M, Eisaki H, Uchida S and Davis J C 2002 *Science* **297** 1148

[33] Avraham N, Reiner J, Kumar-Nayak A, Morali N, Batabyal R, Yan B and Beidenkopf H 2018 *Adv. Mater.* **30** 1707628

[34] Chen H, Yang H, Hu B, Zhao Z, Yuan J, Xing Y, Qian G, Huang Z, Li G, Ye Y, Ma S, Ni S, Zhang H, Yin Q, Gong C, Tu Z, Lei H, Tan H, Zhou S, Shen C, Dong X, Yan B, Wang Z and Gao H J 2021 *Nature* **599** 222